Nonparametric Estimation of DEM Error in Multitemporal InSAR

Hongyu Liang, *Student Member, IEEE*, Lei Zhang, *Senior Member, IEEE*, Zhong Lu, and Xin Li

***Abstract*— Isolating phase residuals due to inaccurate external digital elevation model (DEM) is important in retrieval and interpretation of deformation behavior from interferometric synthetic aperture radar (InSAR) observations. Multitemporal InSAR (MTInSAR), by taking DEM error as a parameter, can make the isolation possible. However, due to the presence of atmospheric artifacts in observations and improper deformation model employed in the observation system, accurate retrieval of DEM error cannot be guaranteed in current MTInSAR techniques. Considering that the DEM error has a fixed spatial pattern and its contribution to interferometric phase-only changes with spatial baselines, we propose here a nonparametric method that can estimate the DEM error in a more robust way. To retrieve signals having a fixed spatial pattern from unwrapped MTInSAR measurements, the independent component analysis (ICA) is used. Experiments with synthetic and real data sets indicate the proposed method is able to estimate DEM error with no *a priori* information about deformation. Moreover, experiments also show that the method can provide a more robust estimation when the observed phase observations are affected by atmospheric delays and/or the number of interferograms used is limited.**

***Index Terms*— Digital elevation model (DEM) error, independent component analysis (ICA), interferometric synthetic aperture radar (InSAR).**

I. Introduction

DIFFERENTIAL interferometric synthetic aperture radar (DInSAR) has been proven to measure ground movement with centimeter-to-millimeter precision on the scale of hundreds of kilometers at a spatial resolution of less than tens of meters. Currently, DInSAR has routinely been used to retrieve land surface deformation caused by either natural or anthropogenic activities, such as earthquakes, volcanism, landslides, and exploitation of groundwater [1]–[4]. However, the accuracy of single-pair interferometry is confined by several factors, i.e., spatial and temporal decorrelation, atmospheric propagation delays, orbital inaccuracy, and topographic errors. To mitigate these adverse effects, multitemporal InSAR (MTInSAR) methods have been developed by leveraging an extensive archive of SAR acquisitions covering the same area, such as persistent scatterer (PS) [5]–[9] and short baseline (SB) [10]–[15] techniques. PS techniques directly work on wrapped phases to extract deformation information from individual points with stable phase quality over the entire observation period. In contrast, the short baseline (SB) methods usually obtain displacement history from the inversion of unwrapped interferograms with small spatial and temporal baselines.

Before using either of these methods to retrieve displacement history, the phase residual due to the digital elevation model (DEM) error should be removed through a linear relation to the spatial baseline of the interferogram. Obviously, inaccurate estimation of DEM error can lead to unexpected phase fluctuation in the interferogram and further distort the retrieval of spatiotemporal behaviors of ground displacement [10], [14], [16]. In the standard PS technique, DEM error is jointly estimated along with the deformation velocity from a wrapped phase difference between two PSs (i.e., arc) [5]. DEM error is also alternatively estimated based on the property of low correlation in space [17], [18]. In SB techniques [e.g., SB subset (SBAS)], DEM error is estimated together with deformation parameters directly from unwrapped phases at coherent points [10], [12], [16], [19]. More recently, alternative SB methods have been developed to estimate DEM error by either parameterizing DEM error together with interval velocities [14], [20] or implementing estimation after phase vector inversion [16], [19]. Although these methods have proved their performance in many applications, the estimation based on a single point or arc is still vulnerable and cannot guarantee accurate DEM error estimates in all cases. As discussed in previous studies [14], [16], [20], [21], the accuracy of estimated DEM error can be affected by the baseline configuration of selected interferograms, interferogram network subsets, atmospheric artifacts, and the discrepancy between modeled and real deformation signals. It is unlikely that current parametric MTInSAR DEM error estimation methods can avoid all these effects.

To tackle the aforementioned problems, we propose a nonparametric MTInSAR estimator for retrieval of DEM error. The rationale is rooted in the fact that DEM error has a deterministic relationship with interferometric phase [22].

Manuscript received July 30, 2018; revised January 11, 2019 and June 17, 2019; accepted July 15, 2019. This work was supported in part by the National Natural Science Foundation of China under Grant 41774023 and Grant 41304011 and in part by the Research Grants Council of Hong Kong under Grant PolyU 152214/14E and Grant 152043/14E. *(Corresponding author: Lei Zhang.)*

H. Liang is with the Department of Land Surveying and Geo-Informatics, The Hong Kong Polytechnic University, Hong Kong (e-mail: allenhongyu.liang@connect.polyu.hk).

L. Zhang was with the Department of Land Surveying and Geo-Informatics, The Hong Kong Polytechnic University, Hong Kong. He is now with the Faculty of Architecture, The University of Hong Kong, Hong Kong (e-mail: lslzhang@hku.hk).

Z. Lu is with the Roy M. Huffington Department of Earth Sciences, South Methodist University, Dallas, TX 75275 USA (e-mail: zhonglu@smu.edu).

X. Li is with the Institute of Geographic Sciences and Natural Resources Research, Chinese Academy of Sciences, Beijing 100101, China (e-mail: vivianyoxi@gmail.com).

Color versions of one or more of the figures in this article are available online at http://ieeexplore.ieee.org.

Digital Object Identifier 10.1109/TGRS.2019.2930802

Unlike other phase contributors (e.g., deformation, atmospheric artifacts, and noise), DEM error has a fixed spatial pattern which is independent with others in space [23]. Starting from the unwrapped interferograms, the proposed estimator can retrieve an accurate DEM error with three steps. In the first step, the multi-temporal unwrapped interferograms are converted to sequential phase vector in the time domain. Second, the independent component analysis (ICA) is applied to decompose the sequential interferogram stack into a collection of spatial distribution functions and associated mixing matrix by maximizing their mutual independence in space. The advantage of using ICA is that it makes no assumption about the spatial–temporal composition of geophysical signals in interferograms and no *a priori* information (such as deformation model and atmospheric delays) is required to constrain the decomposition. Finally, the component contributed by DEM error is sufficiently identified by maximizing the correlation between the corresponding mixing vector and spatial baselines of sequential interferograms. The identified spatial function is converted to the estimated DEM error map by using the least squares (LS). Since the estimation is operated on a scene basis, the map of topographic error for all points in the scene can be simultaneously derived in an extremely efficient way.

The structure of this paper is organized as follows. Section II briefly presents the principle of ICA. In Section III, the nonparametric estimation of DEM error with ICA is described in detail. Section IV verifies the performance of the proposed method by comparing it with conventional methods based on the synthetic data set. Section V is dedicated to the application of the proposed method using a real data set over Dangxiong, China. The conclusion and discussion are addressed in Section VI.

II. Independent Component Analysis

ICA stems from a common assumption that the observed signals can be expressed as a linear combination of statistically independent components, which we refer to as sources. The relationship between the observed signals and the independent sources can be described by [24]

$$\boldsymbol{X} = \boldsymbol{A}\boldsymbol{S} \tag{1}$$

where $\boldsymbol{X}$ is the matrix of observed signals, in which columns correspond to variables and rows correspond to different observations in time series. $\boldsymbol{S}$ is the matrix of sources, where each row represents an independent source. $\boldsymbol{A}$ is denoted as mixing matrix in which each row determines the coefficients of relative contribution of each source to the corresponding row of the observed variable in $\boldsymbol{X}$. As both $\boldsymbol{A}$ and $\boldsymbol{S}$ in (1) are unknown, the equation is underdetermined, indicating extra constraints are required to solve (1) [25]. For ICA, the unique solution is derived by maximizing the mutual independence of estimated sources, more specifically, maximizing non-Gaussianity of sources. This assumption is made based on the central limit theorem (CLT) that indicates the sum of sufficient independent random variables with non-Gaussian distributions tend to follow Gaussian distribution with the increase of variable number. Therefore, a variable being more non-Gaussian has a higher probability to be an independent source. The non-Gaussianity can be quantitatively measured by a number of variables with different properties, such as kurtosis and negentropy. Kurtosis is a fourth-order cumulant that describes the "tailedness" of the probability distribution. For a Gaussian variable with the standard normal distribution, its kurtosis value is three [23], [26]. The kurtosis value is easy to calculate, but it is not a robust measurement due to its sensitivity to outliers. Alternatively, negentropy is more robust, which is estimated based on the information-theoretic quantity of entropy that indicates the Gaussian variable has the largest entropy. In fact, since the computation of negentropy is difficult, a simpler approximation of negentropy is commonly used to assess non-Gaussianity [26], [27].

As a blind source separation technique, ICA is capable of decomposing the mixed signals into several linear and additive components based on the higher statistical moments and cumulants. Its potential has already been widely exploited in remote sensing and geoscience fields, such as denoising GRACE gravity data [28], unmixing hyperspectral satellite images [29], filtering Global Positioning System (GPS) observations [30], and extraction of radiance from high-temperature events (HTEs) time series [31]. Specifically, ICA has also been applied in SAR image processing, including polarimetric SAR (PolSAR) data classification [32], DEM generation [33], and separation of atmospheric noise from InSAR data set [23].

III. Nonparametric MTInSAR Estimator

A. Time-Series Inversion

Given $N+1$ SAR images, M interferometric pairs with high coherence are selected. After phase correction for earth curvature and topographic effect, the M differential interferograms are unwrapped and calibrated with respect to a reference point. To ease the following ICA decomposition, we invert the M interferograms to N sequential phase maps [23]. The time-series inversion has the advantage of reducing the size of interferogram stack, improving the efficiency of following ICA decomposition. Moreover, the inversion can decrease the sensitivity of parameter estimation to interferogram network [16], [21]. A pixel-by-pixel inversion function is defined as follows:

$$\boldsymbol{\delta\phi} = \boldsymbol{B}\boldsymbol{\phi} \tag{2}$$

where $\boldsymbol{\delta\phi} = [\delta\phi^1, \ldots, \delta\phi^M]^T$ is denoted as the known vector of unwrapped phase values of M differential interferograms, $\boldsymbol{\phi} = [\phi^1, \ldots, \phi^N]^T$ represents the unknown vector of phase values of N sequential interferograms in time series, and $\boldsymbol{B}$ is the design matrix to connect original interferograms and sequential phase maps. If the M interferograms belong to a single interferogram subset, (2) can be solved by LS

$$\boldsymbol{\phi} = (\boldsymbol{B}^T\boldsymbol{B})^{-1}\boldsymbol{B}^T\boldsymbol{\delta\phi}. \tag{3}$$

Unfortunately, it is common that the selected interferograms belong to different subsets because of decorrelation effects, leading to an underdetermined linear system. Although singular value decomposition (SVD) [10] and iteratively reweighted LS (IRLS) [34] can provide a unique solution based on

minimum norm of inverted parameters, the constraints' lack of physical meaning might break the linear relation between topographic phase residual and spatial baseline, especially when phase measurements are affected by atmospheric artifacts [21]. Therefore, as an alternative, when there are multiple interferogram subsets, we implement LS in each subset independently and combine the inverted interval interferograms back together. The procedure is described as follows.

1) Identify the subsets of interferogram network.
2) In each subset, determine the number of epoch intervals and build up the inversion model between the original interferograms and the consecutive interval phases from (2) and yield the solution by LS.
3) Repeat 2) for all subsets and combine the solutions into a single matrix.

As a remark, during the inversion, the associated spatial baseline for each consecutive epoch interval should be calculated as well.

B. Decomposition by ICA

After temporal inversion for all selected points, we decompose the sequential interferogram stack into a collection of statistically independent components by ICA. Due to the characteristics of InSAR measurement, each unwrapped interferogram phase can be thought of as the linear mixture of statistically independent sources, which can be expressed as

$$\emptyset^j = \emptyset^j_{\text{defo}} + \emptyset^j_{\text{topo}} + \emptyset^j_{\text{atm}} + \emptyset^j_{\text{orb}} + \emptyset^j_{\text{noise}} \tag{4}$$

where $\emptyset^j$ is the unwrapped phase map of the jth sequential interferogram, $\emptyset^j_{\text{defo}}$ represents the phase component due to the ground movement along the line-of-sight (LOS) direction in the jth time interval, $\emptyset^j_{\text{topo}}$ is denoted as the phase residual due to topographic error, $\emptyset^j_{\text{atm}}$ refers to as the phase component due to variation of atmospheric delays, $\emptyset^j_{\text{orb}}$ is the phase component induced by orbital inaccuracy of SAR satellite, and $\emptyset^j_{\text{noise}}$ represents the processing noise. Phase residual map due to topographic error $\emptyset^j_{\text{topo}}$ is deterministic [22] and it can be modeled by

$$\emptyset^j_{\text{topo}} = \underline{b}^j \boldsymbol{h}^{\varepsilon}, \quad j = 1, 2, \ldots, N$$

with

$$\underline{b}^j = \frac{4\pi}{\lambda} \frac{b^j_{\perp}}{r \sin(\theta)} \tag{5}$$

where $b^j_{\perp}$ represents the spatial baseline of the jth sequential interferogram, λ is the radar wavelength, r is the slant range between SAR sensor and ground surface, θ is the looking angle, and $\boldsymbol{h}^{\varepsilon}$ represents the topographic error map, which is assumed to be static during the whole SAR observation period [10], [16], [19]. It can be deduced from (5), the spatial pattern of topographic error in different time intervals is fixed and the contributed phases are proportional to their perpendicular baselines. This unique feature enables the separation of DEM error from InSAR measurements through ICA by maximizing its spatial independence with other signals. To achieve that, we treat all selected points in each sequential phase map as column vector $\emptyset$. Considering N consecutive phase maps, the matrix of mixed signals in (1) has the form as $\boldsymbol{X} = [\emptyset^1, \ldots, \emptyset^N]^T$. Meanwhile, we expect the matrix of sources in (1) has the form as $\boldsymbol{S} = [S_1, S_2, \ldots, S_i, \ldots]^T$, in which each row represents a spatial distribution of independent sources. $\boldsymbol{X}$ and $\boldsymbol{S}$ are linked by mixing matrix $\boldsymbol{A}$, as shown in (1). It should be noted that before the ICA decomposition, the dimensionality of independent source matrix $\boldsymbol{S}$ is unknown.

In this paper, we utilize the FastICA algorithm [26], [35], [36] to decompose the mixed-signal matrix $\boldsymbol{X}$ and yield the unique solution of mixing matrix $\boldsymbol{A}$ and source matrix $\boldsymbol{S}$. The precursor steps before FastICA include centering and whitening so that the columns of the matrix of mixed signals are transformed into an orthogonal space with reduced noise levels in the data set (see Appendix A). The centering is achieved by subtracting the mean of each column of the mixed-signal matrix $\boldsymbol{X}$ from the matrix itself. Then, the centered matrix is multiplied by a whitening matrix, which is obtained by principal component analysis (PCA) decomposition. The number of principal components retained is related with the dimensionality of independent sources, which is usually unknown in InSAR observation without *a priori* information.

Here, we use optimal singular value hard thresholding (SVHT) [37] to determine the number. The threshold is yielded by

$$\tau_* = 2.858 \cdot d_{\text{med}} \tag{6}$$

where d_{med} is the median eigenvalue of the covariance matrix of centered data in (A3). Thus, the number of principal components retained k is determined by the number of the eigenvalue in the covariance matrix that is larger than the threshold τ_*

$$k = \#(d_j > \tau_*), \quad j = 1, 2, \ldots, N \tag{7}$$

where $\#(\cdot)$ is the number of elements in $(\cdot)$.

After the preprocessing steps, the FastICA algorithm employs a fixed-point iteration scheme to derive the converged solution of mixing matrix $\boldsymbol{A}$ and source matrix $\boldsymbol{S}$ by maximizing the spatial non-Gaussianity of sources. Each mixing vector, which is a row of $\boldsymbol{A}$, defines a projection of the independent sources into the mixed signals. Each column of $\boldsymbol{A}$ defines the relative contributions of the corresponding source into N sequential interferograms. Considering k independent sources derived, the relationship between the N sequential interferograms and the independent sources can be alternatively expressed as a sum of outer products, which is given by

$$\boldsymbol{X} = \sum_{i}^{k} \boldsymbol{a}_{\cdot i} \otimes \boldsymbol{s}_{i\cdot} \tag{8}$$

where $\boldsymbol{s}_{i\cdot}$ represents the spatial distribution of the ith independent source given by the ith row of $\boldsymbol{S}$, $\boldsymbol{a}_{\cdot i}$ represents the vector of relative contribution of corresponding source $\boldsymbol{s}_{i\cdot}$ given by the ith column of $\boldsymbol{A}$, $\otimes$ denotes the outer product. Equation (8) describes how each spatial source is combined to contribute to the total spatiotemporal InSAR data set.

C. DEM Error Estimation

Following (7), once the sequential interferogram data set is divided into k independent components and associated mixing matrix, the source of DEM error can be identified, provided that there is *a priori* information of the spatial distribution function $\boldsymbol{s}_i$. However, since the ICA decomposition is performed in the orthogonal space through centering and whitening procedures, the sign and the magnitude of independent components are ambiguous after decomposition [26]. It is difficult to extract the source of interest directly by inspection of the spatial distribution function. Alternatively, as the coefficient of column vector $\boldsymbol{a}_{\cdot i}$ describes the relative contribution of independent sources to each interferogram in the sequential data set, given the linear relation between DEM error phase residual and spatial baseline described in (5), the column vector $\boldsymbol{a}_{\cdot i}$ corresponding to the independent component of DEM errors can be described as a linear function of spatial baseline of sequential interferograms. In this paper, for the sake of computation efficiency and reliability, we propose two steps to determine the independent component of interest. In the first step, we identify the component of interest by calculating the correlation coefficient between the column vector of mixing matrix $\boldsymbol{A}$ and the spatial baseline for each divided component, that is,

$$\gamma_i = \frac{\sum_{j=1}^{N}(a_{ji}-\overline{\boldsymbol{a}_{\cdot i}})(b_{\perp}^{j}-\overline{b_{\perp}^{\cdot}})}{\sqrt{\sum_{j=1}^{N}(a_{ji}-\overline{\boldsymbol{a}_{\cdot i}})^2\sum_{j=1}^{N}(b_{\perp}^{j}-\overline{b_{\perp}^{\cdot}})^2}}, \quad i=1,2,\ldots,k$$

with

$$\overline{\boldsymbol{a}_{\cdot i}} = \frac{1}{N}\sum_{j=1}^{N} a_{ji}$$

$$\overline{b_{\perp}^{\cdot}} = \frac{1}{N}\sum_{j=1}^{N} b_{\perp}^{j}. \tag{9}$$

The source component of DEM error, which is denoted as the tth component, is expected to have the largest absolute value of correlation coefficient

$$\gamma_t = \max_i\{|\gamma_i|\}, \quad i=1,2,\ldots,k. \tag{10}$$

Once the source of DEM error is initially determined, the contribution of the source of DEM error into the sequential interferogram stack can be expressed as

$$\emptyset_{\text{topo}} = \boldsymbol{a}_{\cdot t} \otimes \boldsymbol{s}_{t\cdot}. \tag{11}$$

Assuming $\boldsymbol{h}^{\varepsilon}$ is the unknown DEM error map for all selected points in the radar scene, combining (5), (8), and (11), we can derive

$$\emptyset_{\text{topo}} = \underline{\boldsymbol{b}}\otimes\boldsymbol{h}^{\varepsilon} = \underline{\boldsymbol{b}}\otimes(f\boldsymbol{s}_{t\cdot}) = (\underline{\boldsymbol{b}}f)\otimes\boldsymbol{s}_{t\cdot}$$

with

$$\underline{\boldsymbol{b}} = [\underline{b}^1,\ldots,\underline{b}^j,\ldots,\underline{b}^N] \tag{12}$$

where f is the conversion coefficient between the vector for spatial baseline factor $\underline{\boldsymbol{b}}$ and the column vector $\boldsymbol{a}_{\cdot t}$ of identified DEM error source, which can be estimated using LS

$$f = (\underline{\boldsymbol{b}}\underline{\boldsymbol{b}}^T)^{-1}\underline{\boldsymbol{b}}\boldsymbol{a}_{\cdot t}^T. \tag{13}$$

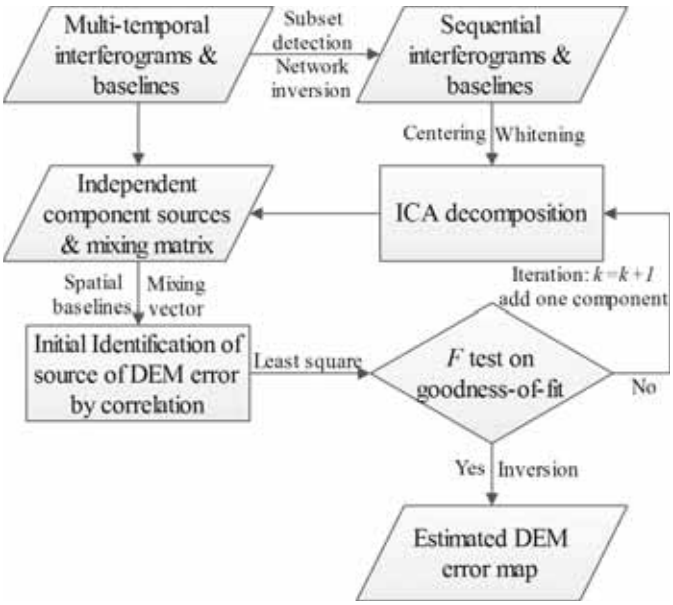

Fig. 1. Workflow of DEM error estimation by the proposed method.

Second, in order to test the statistical significance of component extraction of DEM error, we employ an F test to determine whether the elements of the selected row $\boldsymbol{a}_{t\cdot}$ of $\boldsymbol{A}$ are sufficiently correlated with spatial baselines and further indicate the corresponding source is attributed to topographic error. The F test is described as [38], [39]

$$F = \frac{\sum_{j=1}^{N}\underline{\boldsymbol{b}}^2 f^2}{\sum_{j=1}^{N}(a_{jt}-\underline{\boldsymbol{b}}f)^2}(N-1) \tag{14}$$

where the F statistic follows the F-distribution with $(1, N-1)$ degrees of freedom. Given the significance level of α and degrees of freedom, the critical value of the F-distribution $F_{1,N-1,\alpha}$ is calculated. If $F < F_{1,N-1,\alpha}$, it means that the column vector of the selected components does not significantly fit the linear relation with spatial baselines, leading to a failed estimation of the spatial distribution of DEM error. In this case, the number of principal components retained in (7) is reevaluated by adding one. If $F > F_{1,N-1,\alpha}$, it indicates that the mixing vector of the selected component is sufficiently correlated with spatial baselines regardless of the presence of other confounding signals (e.g., deformation, atmospheric artifacts, and orbital inaccuracy) and the determined component can be further converted to DEM error. Combining (12) and (13), the unknown DEM error map is obtained by

$$\boldsymbol{h}^{\varepsilon} = f\boldsymbol{s}_{t\cdot}. \tag{15}$$

As a summary, Fig. 1 depicts the involved steps for the whole proposed nonparametric DEM error estimation process.

IV. Synthetic Data Tests

To evaluate the performance of the proposed DEM error estimator, a set of simulation tests are conducted. During these tests, a total of 23 SAR acquisitions from C-band sensor with a wavelength of 5.62 cm are used, where the spatial and temporal baseline information is retrieved from

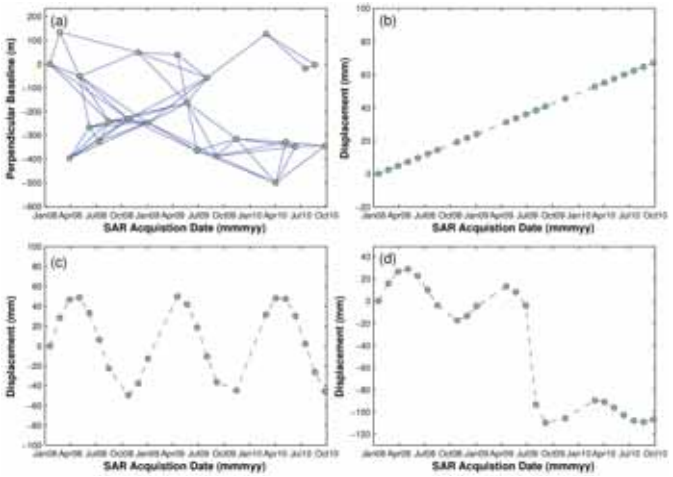

Fig. 2. (a) Network plot of selected interferograms. Simulated (b) linear, (c) periodic, and (d) complex deformation models in time series.

real Envisat/ASAR data set (Frame 2925, Track 170) over Los Angeles Basin, CA, USA. From the SAR images, we select 250 000 coherent points and generate 63 interferograms with spatial and temporal baselines shorter than 245 m and 280 days, respectively. The network of selected interferograms is shown in Fig. 2(a). We assume that the phase ramps due to satellite orbital inaccuracy have been removed from interferograms, which, in real cases, can be done by using the method proposed in [40]. Thus, the signals considered in the synthetic interferograms include ground deformation, DEM error, atmospheric delays, and noise. For the sake of simplicity, the spatial pattern of deformation is created by using the peak function in MATLAB. Meanwhile, three kinds of deformation behavior in time series are simulated, i.e., linear [Fig. 2(b)], periodic [Fig. 2(c)], and complex ones [Fig. 2(d)]. The DEM error map is produced by employing fractal surface with a fractal dimension of three and the error values distribute from −30 to 30 m. The atmospheric delays in each SAR acquisition are generated with the fractal dimension of 2.2 with the maximum delay value varying from 0 to 3.5 rad. In addition, we add the thermal noise into the interferogram with a mean of zero rad and a standard deviation (STD) of 0.1 rad. As an example, Fig. 3 depicts the spatial pattern of one synthetic interferogram.

To assess the effectiveness of the proposed method under different conditions, we independently vary one factor while fixing the effects of other simulated parameters. Moreover, we compare the new method with three existing methods for DEM error estimation, i.e., original SBAS [10], Fattahi's [16], and Samsonov's methods [14]. The accuracy of estimated DEM error is quantitively described by using the root-mean-square error (RMSE) between estimated and simulated DEM errors

$$\boldsymbol{h}^{\varepsilon}_{\text{rmse}} = \sqrt{\frac{1}{\text{Num}}\sum_{i=1}^{\text{Num}}\left(\boldsymbol{h}^{\varepsilon}_{\text{est}} - \boldsymbol{h}^{\varepsilon}_{\text{true}}\right)^2} \tag{16}$$

where $\boldsymbol{h}^{\varepsilon}_{\text{est}}$ and $\boldsymbol{h}^{\varepsilon}_{\text{true}}$ are the estimated and simulated DEM error maps, respectively, and Num represents the number of coherent points.

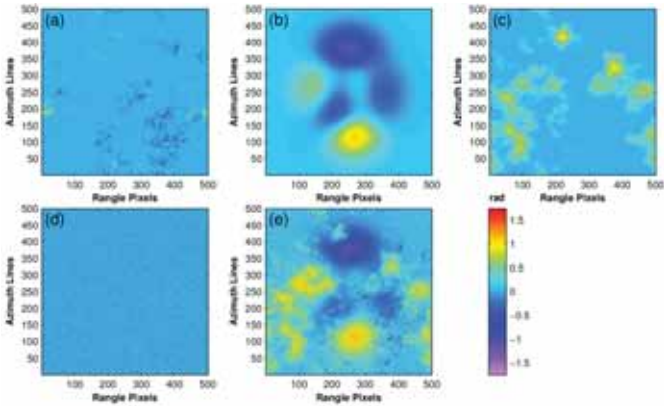

Fig. 3. Schematic realization of the generation of the synthetic interferogram. (a) DEM error. (b) Deformation. (c) Atmospheric delay. (d) Thermal noise. (e) Final synthetic interferogram after phase unwrapping (perpendicular baseline 85 m and temporal baseline 280 days).

A. Effect of Deformation Models

We first identify the performance of the proposed DEM error estimator with different deformation models. Three sets of interferograms are created with different temporal behaviors of surface displacement (i.e., linear, periodic, and complex). Atmospheric delays with a maximum variation of 1.0 rad are added into the synthetic interferograms. After the phase unwrapping process, the DEM error is estimated by four methods (i.e., original SBAS, Samsonov's, Fattahi's, and the proposed methods). The results are shown in Fig. 4. It can be seen that when the simulated deformation behavior is linear, the four methods obtain consistent results with the simulated values. This is because the simple displacement time series can be well described by the cubic polynomial in [10] and [16] and the phase interval velocities in [14]. On the other hand, when the simulated deformation behavior is periodic, estimation results from the original SBAS, Fattahi's, and Samsonov's methods have discrepancies with the simulated DEM error map. These differences become more obvious when the simulated deformation behavior is complex. The estimation error in the conventional methods occurs mainly due to a discrepancy between the real deformation and the models used. By contrast, the proposed method gives a stable and satisfactory estimation of DEM error regardless of the temporal behavior of deformation, indicating the proposed method is insensitive to the unknown fluctuation of displacements in time series.

B. Effect of Atmospheric Artifacts

We also consider the effects of atmospheric delays on the proposed estimator in different deformation scenarios. To evaluate the effects, in each deformation scenario, atmospheric delays with eight levels of maximum variation are added into the synthetic interferograms with the same level of DEM error and thermal noise. We conduct the estimation and calculate RMSE between the estimated and simulated DEM errors. Fig. 5 shows the comparison of RMSE variation derived by four methods. As expected, in all deformation scenarios, the proposed method has the lowest RMSE with the increase in the atmospheric delay level. Compared with conventional

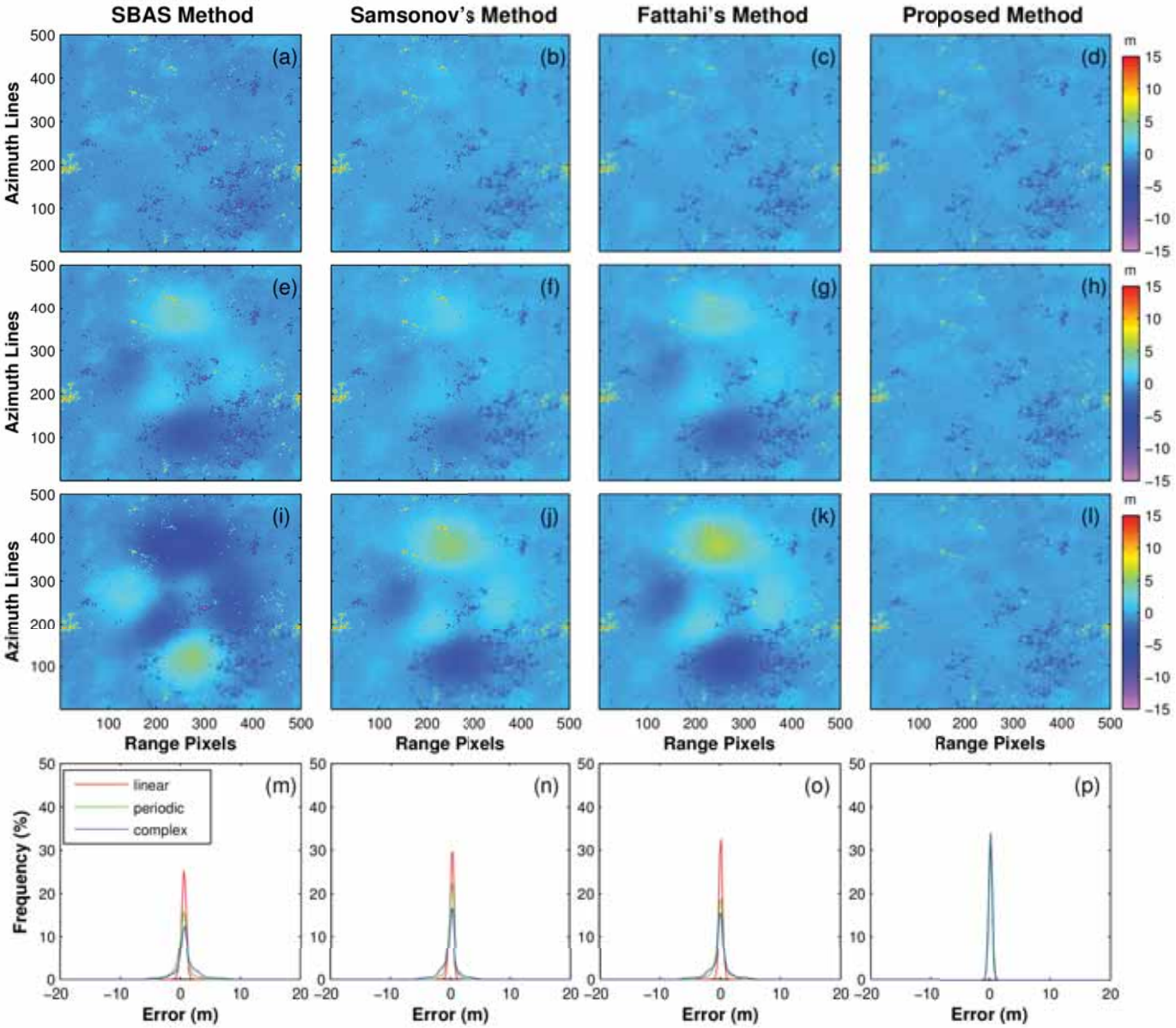

Fig. 4. Effect of simulated deformation input on DEM error estimation by four methods. The first three rows represent the estimated DEM error by four methods when simulated deformation models are (a)–(d) linear, (e)–(h) periodic, and (i)–(l) complex, respectively. The fourth row shows the error histograms between simulated and estimated DEM errors. In (p), three histogram curves (i.e., red, green, and blue lines) have overlapped each other, indicating that the proposed approach is almost immune to the bias raised by improper deformation model. (m)–(p) Fourth row shows the error histograms between simulated and estimated DEM errors.

methods, the proposed method has the lowest sensitivity to the atmospheric contamination.

C. Effect of Maximum Spatial Baseline

To further assess the sensitivity of the maximum spatial baseline to DEM error estimation, we scale the spatial baselines of selected interferograms by varying the coefficient from 0.1 to 2. Based on the scaled baselines, we generate 20 sets of interferograms, where each data set contains the same level of DEM error, deformation, atmospheric delays, and thermal noise. We use four methods to retrieve the map of DEM error from the unwrapped interferograms and calculate RMSE as the function of a maximum spatial baseline of each data set. As shown in Fig. 6, the RMSEs of estimated DEM error decrease with the increase in the maximum value of spatial baseline, suggesting that the use of large baselines can improve the accuracy of estimated DEM errors. On the other hand, the tendency of future satellites with shorter spatial baselines imposes a challenge on the accuracy of DEM error estimation. The results of the proposed method suggest despite the maximum spatial baseline of 50 m, the RMSE can reach up to 2 m, providing a possible solution of the DEM error estimation for the further satellite missions.

D. Effect of Interferogram Number and Subset

We finally test the effects of interferogram number and subset on the DEM error estimation. As described in [21], more interferograms mean more observations, which can

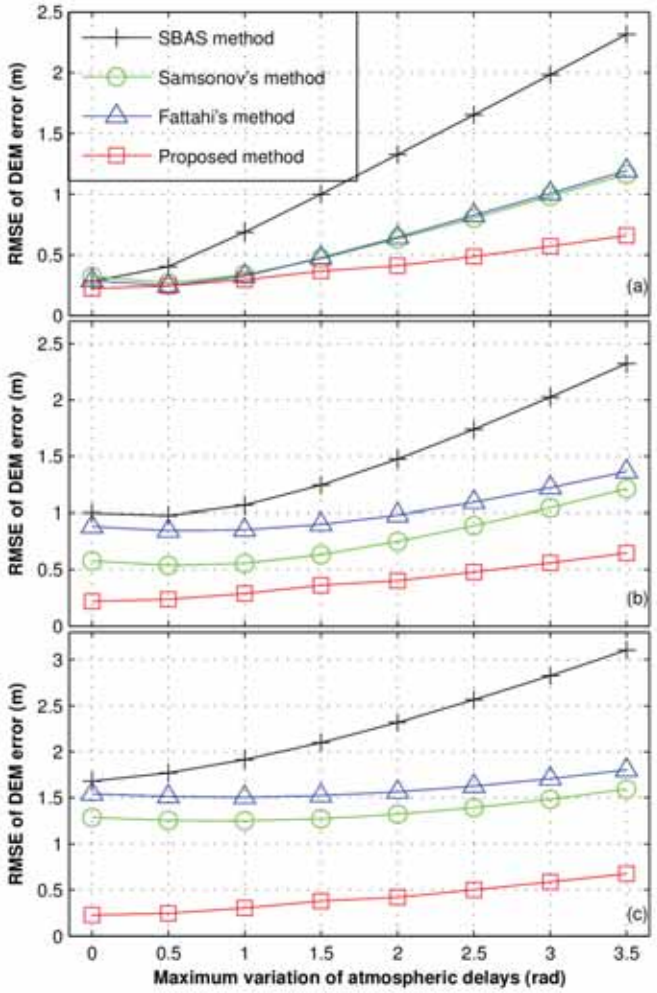

Fig. 5. Effect of atmospheric delays on DEM error estimation by four methods with three deformation inputs. Deformation models are (a) linear, (b) periodic, and (c) complex ones, respectively.

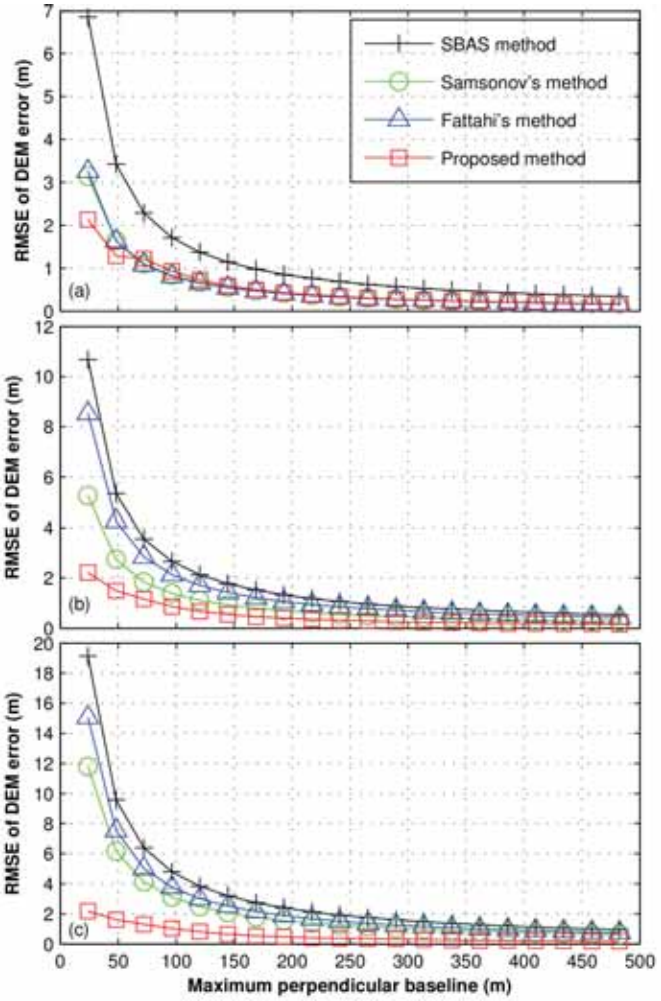

Fig. 6. Effects of spatial baseline threshold on DEM error estimation by four methods with three deformation inputs. Deformation models are (a) linear, (b) periodic, and (c) complex ones, respectively.

improve the accuracy of DEM error estimation. The existence of subsets might lead to a biased estimation, especially when the phase observations include unmodeled displacement and atmospheric delays in time series. To assess the impacts, we extend the thresholds of spatial and temporal baselines to 350 m and 350 days, respectively, and generate 106 interferometric pairs. The same level of DEM error, deformation, atmospheric delays, and thermal noise are converted to phase components and added into the interferograms. We then randomly select interferograms with the selection number ranging from 10 to 105. For each selection number, there are theoretically various combinations; we repeat the selection 100 times without replacement. The DEM error map and the RMSE value are computed based on the selected interferograms. The mean value of RMSE for each selection number represents the overall estimation sensitivity to the number of interferograms, whereas the STD of RMSE for each selection number reflects the stability of the algorithm to interferogram configuration (i.e., subset and baseline distributions). The effects of the interferogram number and subset are illustrated in Fig. 7, where the mean and STD values of RMSE are plotted as the functions of the sampling number, respectively. As shown in Fig. 7 (Left) and (Right), when the selection number is small, the mean and STD values of RMSE significantly decrease with increase in the number of interferograms, demonstrating the estimation of DEM errors is affected by the number of observations. While when the sampling number is large, the RMSEs from the four methods flatten out gradually. In particular, the convergence speed of the new method is the fastest among the four methods, and the mean and STD values of RMSE are the lowest when deformation has periodic or complex characteristics. The test demonstrates that in the case of a small number of interferograms or interferogram subsets, the proposed method is notably superior to the existing methods.

In short summary, we have assessed the performance of the new method and compared it with the existing methods under various environments. The factors we have considered include deformation model, atmospheric contamination, maximum of baseline, and interferogram configuration. The results from synthetic tests reveal that the new method provides a more robust way to estimate the DEM error when the observations suffer the aforementioned effects. To explain the phenomena, conventional methods estimate DEM error from a single point

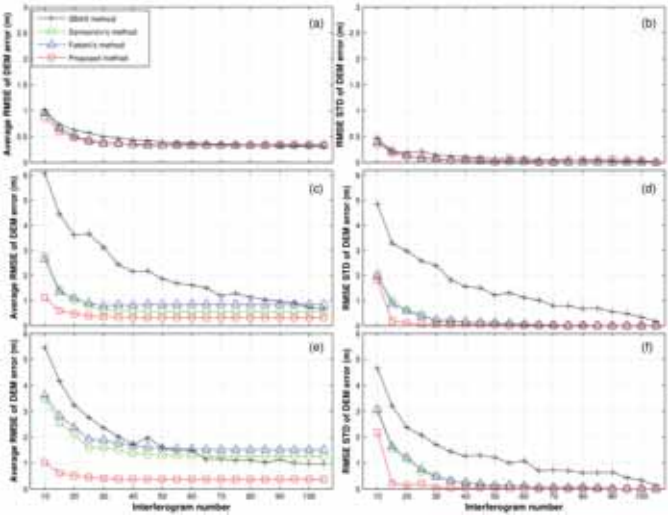

Fig. 7. Effect of interferogram number and subset on DEM error estimation by four methods with three deformation inputs. (Left) The variation in average RMSE between estimated and simulated DEM error by four methods. (Right) The STD of RMSE. Deformation models are (a) and (b) linear, (c) and (d) periodic, and (e) and (f) complex ones, respectively.

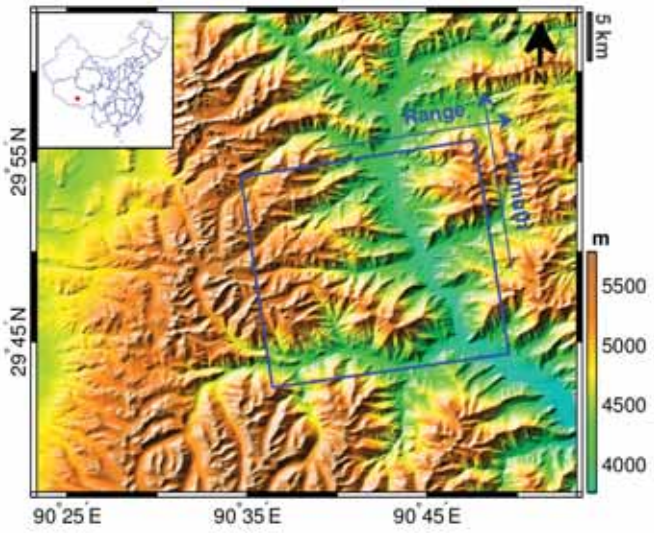

Fig. 8. Shaded-relief map of the study area over Dangxiong, China. Blue solid box: the study area covered by ascending ALOS/PALSAR images (Track 500, Frame 580). The insert map shows the location of the study area in China.

in one dimension, which are more prone to the unexpected phase fluctuations (e.g., unmodeled deformation, atmospheric delay, and network connectivity). However, the new method directly extracts the map of DEM error from the sequential interferogram stack in 2-D space, which operates based on two reasonable assumptions that DEM error is spatially independent with other signals and the induced phase residual in interferograms only varies with the spatial baselines. By considering the 2-D independence and high correlation with spatial baseline, our estimator is much less vulnerable to the signal fluctuation.

V. Real Data Test

To test the algorithm with real data, processing is conducted using data acquired over Dangxiong, China from December 29, 2006 to January 6, 2010 (Fig. 8). A set of nine

TABLE I
Interferometric Pair Baseline Information

Interferometric pair (yyyymmdd)	Perpendicular baseline (m)	Temporal baseline (day)
20061229-20090103	406	736
20071001-20080101	192	92
20071001-20091006	-538	736
20071001-20100106	-290	828
20080101-20100106	-483	736
20080703-20090218	-462	230
20080703-20090821	210	414
20080703-20091006	566	460
20090103-20090218	395	46
20090821-20091006	356	46
20091006-20100106	248	92

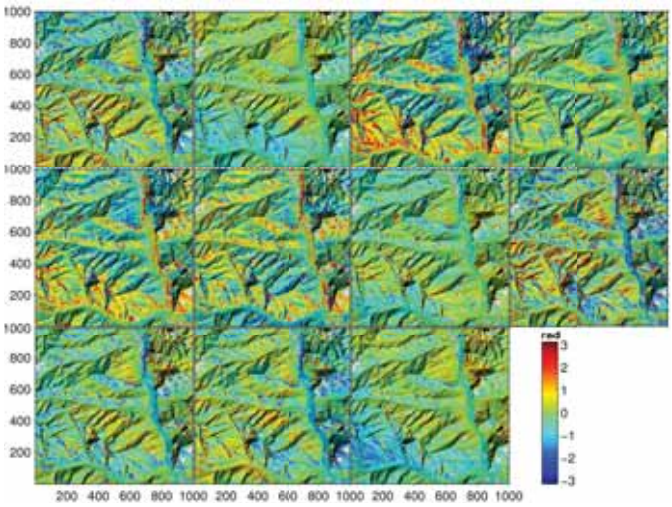

Fig. 9. Wrapped interferograms before correcting DEM error.

ALOS/PALSAR images is used to generate 11 interferograms with the temporal and spatial baselines less than 830 days and 550 m, respectively (see Table I). During the InSAR processing, 1-arc-s ASTER GDEM is used to remove the topographic phase. Accounting for the effects of layover and shadow in mountainous areas, pixels in interferograms suffering from geometric distortions are detected and eliminated.

Fig. 9 shows the interferograms before DEM error correction. Although ASTER GDEM has a vertical accuracy of 15 m in mountainous areas [41], the DEM error in this area is still apparent, hampering the extraction of deformation pattern. After the DEM error correction by using the developed algorithm, the corrected interferograms are shown in Fig. 10. We can see that the phase residual caused by DEM error has been effectively removed. The spatial pattern of the landslide can be identified from the refined interferograms (i.e., the areas in red), benefiting the further interpretation of landslide displacement behavior.

To further demonstrate the stability of our approach in the presence of atmospheric delays, we apply the proposed method to estimate DEM error from interferograms before and after correcting height-dependent atmospheric delays, respectively, and compare the results with the estimation from the conventional methods (i.e., SBAS, Fattahi's method, and Samsonov's method). To remove the height-dependent tropospheric delays,

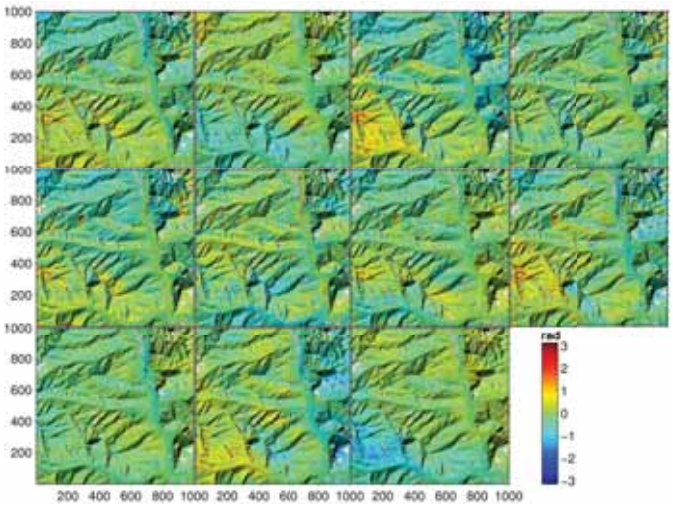

Fig. 10. Wrapped interferograms after correcting DEM error.

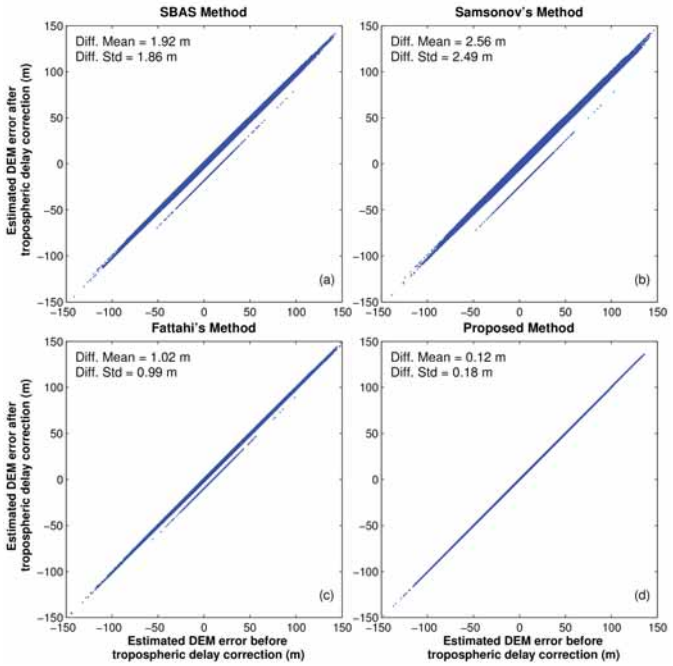

Fig. 11. Comparison of estimated DEM error before and after height-dependent atmospheric delays correction by four methods.

we fit a linear relationship between the unwrapped phase and the local elevation [42]. Fig. 11 presents the comparison of estimated DEM error before and after height-dependent atmospheric delays correction. It is clear that the proposed method can derive stable results despite atmospheric delays, suggesting that the developed method is robust to atmospheric contamination.

From a point view of computation load, since our method directly extracts the spatial pattern of DEM error, the estimation and correction are more efficient for interferogram stacks. More impressively, the performance of the proposed estimator is still satisfied when the number of available interferograms is small. In this real data case, it only takes 4.9 s to obtain the DEM error map from 957 982 points in 11 ALOS/PALSAR interferograms using MATLAB software with an Intel i7 3.6-GHz CPU.

VI. Conclusion and Discussion

In this paper, we have presented a new DEM error estimation method for MTInSAR data sets. This method uses ICA to retrieve independent components of DEM error from the sequential interferograms and perform estimation in a spatial domain. This distinguishes the estimator from the existing methods that derive the parameters of interest based on pixel-by-pixel or arc-by-arc estimation. Distinct advantages of this method are that no *a priori* information of a deformation model in time series is required, and it is largely immune to atmospheric contamination and limitations in baseline configuration.

Results of extensive tests using both synthetic and real data sets have shown that this method works well under various situations and provides more stable and accurate estimation results compared with the existing approaches. Accurate separation of DEM error provides a solid basis for subsequent retrieval of deformation time series in MTInSAR.

It should be pointed out that although ICA can be applied to decompose multitemporal interferograms, the specific decomposition based on mutual independence could fail in some situations. The failure could be attributed to a small number of observations in space or the existence of high-level noise and outliers in observations [26]. Therefore, future work will focus on how to improve the estimation performance in areas with sparse coherent points and possible phase unwrapping errors due to decorrelation.

Appendix

This appendix is dedicated to a more detailed description of the FastICA algorithm, including preprocessing and decomposition, and its application to sequential interferograms. We refer the reader to the survey of FastICA [26], [35], [36] for a deeper understanding. Provided that the observation matrix X is formed by N sequential interferograms, the centered observation matrix X_C is calculated by

$$\boldsymbol{X}_C = \boldsymbol{X} - \overline{\boldsymbol{X}} \tag{A1}$$

where $\overline{\boldsymbol{X}}$ is a matrix in which each column equals the mean of the corresponding column in $\boldsymbol{X}$ so that each column of the centered matrix X_C has a zero-mean value. In order to whiten the observation matrix, the centered matrix is used to generate the covariance matrix $\boldsymbol{C}_X$ as

$$\boldsymbol{C}_X = \frac{1}{N}\boldsymbol{X}_C\boldsymbol{X}_C^T \tag{A2}$$

where N is the number of the sequential interferograms. The covariance matrix is then decomposed by maximizing a total variance of the projection based on PCA

$$\boldsymbol{C}_X = \boldsymbol{E}\boldsymbol{D}\boldsymbol{E}^T = \sum_{j=1}^{N} d_j \cdot \boldsymbol{e}_j \cdot \boldsymbol{e}_j^T \tag{A3}$$

where $\boldsymbol{e}$ and $\boldsymbol{E}$ are the eigenvector and eigenvector matrix, and d and $\boldsymbol{D}$ are eigenvalue and eigenvalue matrix, respectively.

The whitening matrix is calculated by

$$\boldsymbol{Q} = (\boldsymbol{E}\boldsymbol{D}^{-1/2}\boldsymbol{E}^{T})_{k} \tag{A4}$$

where k is the number of retained principal components. In this paper, we use SVHT [37] to determine the number. The whitened observation matrix Z is derived by

$$\boldsymbol{Z} = \boldsymbol{Q}\boldsymbol{X}_{C}. \tag{A5}$$

Once the observation matrix has been centered and whitened, the FastICA algorithm uses a fixed-point iteration to derive the source matrix and mixing matrix by maximizing spatial non-Gaussian of sources

$$\boldsymbol{Z} = \tilde{\boldsymbol{A}}\tilde{\boldsymbol{S}} \tag{A6}$$

where $\tilde{\boldsymbol{A}}$ and $\tilde{\boldsymbol{S}}$ are the mixing matrix and the source matrix of centered and whitened observations, respectively. The centered observation matrix can also be expressed as a combination of source matrix and mixing matrix by using the inverse operation of whitening process

$$\boldsymbol{X}_{C} = \boldsymbol{Q}^{+}\tilde{\boldsymbol{A}}\tilde{\boldsymbol{S}} = \boldsymbol{A}\tilde{\boldsymbol{S}}$$

with

$$\boldsymbol{A} = \boldsymbol{Q}^{+}\tilde{A} \tag{A7}$$

where $\boldsymbol{Q}^{+}$ is the pseudoinverse of whitening matrix $\boldsymbol{Q}$. The original observation matrix can be expressed as

$$\boldsymbol{X} = \boldsymbol{A}\tilde{\boldsymbol{S}} + \boldsymbol{A}\boldsymbol{A}^{-1}\overline{\boldsymbol{X}} = \boldsymbol{A}(\tilde{\boldsymbol{S}} + \boldsymbol{A}^{-1}\overline{\boldsymbol{X}}) = \boldsymbol{A}\boldsymbol{S}$$

with

$$\boldsymbol{S} = \tilde{\boldsymbol{S}} + \boldsymbol{A}^{-1}\overline{\boldsymbol{X}} \tag{A8}$$

where $\boldsymbol{A}$ and $\boldsymbol{S}$ are the mixing matrix and the source matrix of the original observation matrix, respectively.

ACKNOWLEDGMENT

The authors would like to thank the Japan Aerospace Exploration Agency (JAXA) for providing the ALOS/PALSAR data via Project P1246 and Project P3381. They would also like to thank Dr. P. Lundgren and another anonymous reviewer for their constructive suggestions.

REFERENCES

[1] Y. Fialko, "Evidence of fluid-filled upper crust from observations of postseismic deformation due to the 1992 M_w7. 3 Landers earthquake," *J. Geophys. Res. Solid Earth*, vol. 109, p. B8, Aug. 2004.

[2] Z. Lu and D. Dzurisin, *InSAR Imaging of Aleutian Volcanoes: Monitoring a Volcanic Arc From Space*. New York, NY, USA: Springer, 2014.

[3] Q. Sun, L. Zhang, X. Ding, J. Hu, Z. W. Li, and J. J. Zhu, "Slope deformation prior to Zhouqu, China landslide from InSAR time series analysis," *Remote Sens. Environ.*, vol. 156, pp. 45–57, Jan. 2015.

[4] L. Zhang, Z. Lu, X. Ding, H.-S. Jung, G. Feng, and C.-W. Lee, "Mapping ground surface deformation using temporarily coherent point SAR interferometry: Application to Los Angeles Basin," *Remote Sens. Environ.*, vol. 117, pp. 429–439, Feb. 2012.

[5] A. Ferretti, C. Prati, and F. Rocca, "Permanent scatterers in SAR interferometry," *IEEE Trans. Geosci. Remote Sens.*, vol. 39, no. 1, pp. 8–20, Jan. 2001.

[6] A. Hooper, P. Segall, and H. Zebker, "Persistent scatterer interferometric synthetic aperture radar for crustal deformation analysis, with application to Volcán Alcedo, Galápagos," *J. Geophys. Res.*, vol. 112, p. B7, Jul. 2007.

[7] B. M. Kampes, *Radar Interferometry: Persistent Scatterer Technique*. New York, NY, USA: Springer, 2006.

[8] L. Zhang, X. Ding, and Z. Lu, "Modeling PSInSAR time series without phase unwrapping," *IEEE Trans. Geosci. Remote Sens.*, vol. 49, no. 1, pp. 547–556, Jan. 2011.

[9] M. Costantini, S. Falco, F. Malvarosa, F. Minati, F. Trillo, and F. Vecchioli, "Persistent scatterer pair interferometry: Approach and application to COSMO-SkyMed SAR data," *IEEE J. Sel. Topics Appl. Earth Observ. Remote Sens.*, vol. 7, no. 7, pp. 2869–2879, Jul. 2014.

[10] P. Berardino, G. Fornaro, R. Lanari, and E. Sansosti, "A new algorithm for surface deformation monitoring based on small baseline differential SAR interferograms," *IEEE Trans. Geosci. Remote Sens.*, vol. 40, no. 11, pp. 2375–2383, Nov. 2002.

[11] D. A. Schmidt and R. Bürgmann, "Time-dependent land uplift and subsidence in the Santa Clara valley, California, from a large interferometric synthetic aperture radar data set," *J. Geophys. Res. Solid Earth*, vol. 108, p. B9, Sep. 2003.

[12] R. Lanari, O. Mora, M. Manunta, J. J. Mallorquí, P. Berardino, and E. Sansosti, "A small-baseline approach for investigating deformations on full-resolution differential SAR interferograms," *IEEE Trans. Geosci. Remote Sens.*, vol. 42, no. 7, pp. 1377–1386, Jul. 2004.

[13] O. Mora, J. J. Mallorqui, and A. Broquetas, "Linear and nonlinear terrain deformation maps from a reduced set of interferometric SAR images," *IEEE Trans. Geosci. Remote Sens.*, vol. 41, no. 10, pp. 2243–2253, Oct. 2003.

[14] S. Samsonov, "Topographic correction for ALOS PALSAR interferometry," *IEEE Trans. Geosci. Remote Sens.*, vol. 48, no. 7, pp. 3020–3027, Jul. 2010.

[15] P. Blanco-Sánchez, J. J. Mallorquí, S. Duque, and D. Monells, "The coherent pixels technique (CPT): An advanced DInSAR technique for nonlinear deformation monitoring," in *Earth Sciences Mathematics:*, vol. 1, A. G. Camacho, J. I. Díaz, and J. Fernández, Eds. Basel, Switzerland: Birkhäuser Verlag, 2008, pp. 1167–1193.

[16] H. Fattahi and F. Amelung, "DEM error correction in InSAR time series," *IEEE Trans. Geosci. Remote Sens.*, vol. 51, no. 7, pp. 4249–4259, Jul. 2013.

[17] A. Hooper, H. Zebker, P. Segall, and B. Kampes, "A new method for measuring deformation on volcanoes and other natural terrains using InSAR persistent scatterers," *Geophys. Res. Lett.*, vol. 31, p. 23, Dec. 2004.

[18] G. Ducret, M.-P. Doin, R. Grandin, C. Lasserre, and S. Guillaso, "Dem corrections before unwrapping in a Small Baseline strategy for InSar time series analysis," *IEEE Geosci. Remote Sens. Lett.*, vol. 11, no. 3, pp. 696–700, Jul. 2014.

[19] A. Pepe, A. B. Ortiz, P. R. Lundgren, P. A. Rosen, and R. Lanari, "The Stripmap–ScanSAR SBAS approach to fill gaps in stripmap deformation time series with ScanSAR data," *IEEE Trans. Geosci. Remote Sens.*, vol. 49, no. 12, pp. 4788–4804, Dec. 2011.

[20] S. Samsonov, M. van der Kooij, and K. Tiampo, "A simultaneous inversion for deformation rates and topographic errors of DInSAR data utilizing linear least square inversion technique," *Comput. Geosci.*, vol. 37, no. 8, pp. 1083–1091, Aug. 2011.

[21] Y. Du, L. Zhang, G. Feng, Z. Lu, and Q. Sun, "On the accuracy of topographic residuals retrieved by MTInSAR," *IEEE Trans. Geosci. Remote Sens.*, vol. 55, no. 2, pp. 1053–1065, Feb. 2017.

[22] P. S. Agram and M. Simons, "A noise model for InSAR time series," *J. Geophys. Res., Solid Earth*, vol. 120, no. 4, pp. 2752–2771, 2015.

[23] S. K. Ebmeier, "Application of independent component analysis to multitemporal InSAR data with volcanic case studies," *J. Geophys. Res. Solid Earth*, vol. 121, no. 12, pp. 8970–8986, Dec. 2016.

[24] P. Comon, "Independent component analysis, a new concept?" *Signal Process.*, vol. 36, no. 3, pp. 287–314, Apr. 1994.

[25] D. Skillicorn, *Understanding Complex Datasets: Data Mining With Matrix Decompositions*. New York, NY, USA: Chapman and Hall/CRC, 2007.

[26] A. Hyvärinen and E. Oja, "Independent component analysis: Algorithms and applications," *Neural Netw.*, vol. 13, nos. 4–5, pp. 411–430, Jun. 2000.

[27] A. Hyvärinen, "New approximations of differential entropy for independent component analysis and projection pursuit," in *Proc. Adv. Neural Inf. Process. Syst.*, vol. 10. Cambridge, MA, USA: MIT Press, 1998, pp. 273–279.

[28] F. Frappart, G. Ramillien, M. Leblanc, S. O. Tweed, M.-P. Bonnet, and P. Maisongrande, "An independent component analysis filtering approach for estimating continental hydrology in the GRACE gravity data," *Remote Sens. Environ.*, vol. 115, no. 1, pp. 187–204, Jan. 2011.

[29] J. M. P. Nascimento and J. M. Bioucas Dias, "Does independent component analysis play a role in unmixing hyperspectral data?" *IEEE Trans. Geosci. Remote Sens.*, vol. 43, no. 1, pp. 175–187, Jan. 2005.
[30] B. Liu, W. Dai, W. Peng, and X. Meng, "Spatiotemporal analysis of GPS time series in vertical direction using independent component analysis," *Earth, Planets Space*, vol. 67, no. 1, p. 189, Dec. 2015.
[31] T. Barnie and C. Oppenheimer, "Extracting high temperature event radiance from satellite images and correcting for saturation using independent component analysis," *Remote Sens. Environ.*, vol. 158, pp. 56–68, Mar. 2015.
[32] N. Besic, G. Vasile, J. Chanussot, and S. Stankovic, "Polarimetric incoherent target decomposition by means of independent component analysis," *IEEE Trans. Geosci. Remote Sens.*, vol. 53, no. 3, pp. 1236–1247, Mar. 2014.
[33] P. Ballatore, "Extracting digital elevation models from SAR data through independent component analysis," *Int. J. Remote Sens.*, vol. 32, no. 13, pp. 3807–3817, Jul. 2011.
[34] T. R. Lauknes, H. A. Zebker, and Y. Larsen, "InSAR deformation time series using anL_1-norm small-baseline approach," *IEEE Trans. Geosci. Remote Sens.*, vol. 49, no. 1, pp. 536–546, Jan. 2011.
[35] A. Hyvärinen, "Fast and robust fixed-point algorithms for independent component analysis," *IEEE Trans. Neural Netw.*, vol. 10, no. 3, pp. 626–634, May 1999.
[36] A. Hyvärinen and E. Oja, "A fast fixed-point algorithm for independent component analysis," *Neural Comput.*, vol. 9, no. 7, pp. 1483–1492, Jul. 1997.
[37] M. Gavish and D. L. Donoho, "The optimal hard threshold for singular values is $4/\sqrt{3}$," *IEEE Trans. Inf. Theory*, vol. 60, no. 8, pp. 5040–5053, Aug. 2014.
[38] G. K. Kanji, *100 Statistical Tests*. 3rd ed. London, U.K.: SAGE Publications Ltd, 2006, p. 256.
[39] J. G. Eisenhauer, "Regression through the Origin," *Teach. Statist.*, vol. 25, no. 3, pp. 76–80, 2003.
[40] L. Zhang, X. Ding, Z. Lu, H.-S. Jung, J. Hu, and G. Feng, "A novel multitemporal InSAR model for joint estimation of deformation rates and orbital errors," *IEEE Trans. Geosci. Remote Sens.*, vol. 52, no. 6, pp. 3529–3540, Jun. 2014.
[41] T. Tachikawa, M. Kaku, A. Iwasaki, D. Gesch, M. Oimoen, and Z. Zhang, "ASTER global digital elevation model version 2-summary of validation results," in *NASA Land Processes Distributed Active Archive Center & Joint Japan US ASTER Science Team*. Sioux Falls, SD, USA: USGS/Earth Resources Observation and Science (EROS) Center, 2011.
[42] M.-P. Doin, C. Lasserre, G. Peltzer, O. Cavalié, and C. Doubre, "Corrections of stratified tropospheric delays in SAR interferometry: Validation with global atmospheric models," *J. Appl. Geophys.*, vol. 69, no. 1, pp. 35–50, Sep. 2009.

Hongyu Liang (S'18) was born in Bazhong, China, in 1991. He received the B.S. degree from Southwest Jiaotong University, Chengdu, China, in 2013, and the M.Sc. degree in geomatics from The Hong Kong Polytechnic University, Hong Kong, in 2013, where he is currently pursuing the Ph.D. degree with the Department of Land Surveying and Geo-Informatics.

His research interests include estimation theory and advanced processing developments for multitemporal synthetic aperture radar (SAR) interferometry and deformation monitoring.

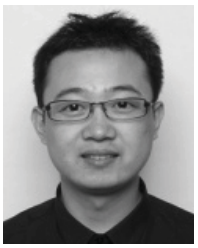

Lei Zhang (S'08–M'11–SM'18) was born in Yantai, China, in 1981. He received the M.Sc. degree from Tongji University, Shanghai, China, in 2007, and the Ph.D. degree in geodesy and geodynamics from The Hong Kong Polytechnic University, Hong Kong, in 2011. His M.Sc. thesis was on fault-slip inversion with interferometric synthetic aperture radar (SAR) and global positioning system (GPS) data based on a triangular dislocation model.

From 2012 to 2018, he was a Research Assistant Professor (RAP) with the Department of Land Surveying and Geo-Informatics, The Hong Kong Polytechnic University. Since 2019, he has been an RAP with the Faculty of Architecture, The University of Hong Kong, Hong Kong. His research interests include developing advanced processing techniques for SAR data and the application of multitemporal interferometric analysis on the retrieval of urban morphology, ground displacement, and geophysical parameters, with an emphasis on natural/metrological hazard monitoring and mitigation.

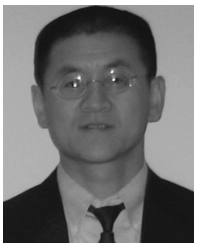

Zhong Lu received the B.S. and M.S. degrees from Peking University, Beijing, China, in 1989 and 1992, respectively, and the Ph.D. degree from the University of Alaska Fairbanks, Fairbanks, AK, USA, in 1996.

From 1997 to 2013, he was a Physical Scientist with United States Geological Survey, Vancouver, WA, USA. He is currently a Professor and the Endowed Shuler-Foscue Chair with the Roy M. Huffington Department of Earth Sciences, Southern Methodist University, Dallas, TX, USA. He has authored or coauthored more than 180 peer-reviewed journal articles and book chapters focused on interferometric synthetic aperture radar (InSAR) techniques and applications, and a book *InSAR Imaging of Aleutian Volcanoes: Monitoring a Volcanic Arc from Space* (Springer, 2014). His research interests include the technique developments of InSAR processing and their applications to the study of volcano, landslide, and coastal processes, among others.

Dr. Lu has been a member of NASA-India SAR Science Team since 2012, a Senior Associate Editor of *Remote Sensing* and *Frontier in Earth Sciences*, and a member of Editorial Boards of the *International Journal of Image and Data Fusion* and *Geomatics, Natural Hazards and Risk*.

Xin Li was born in Tai'an, Shandong, China, in 1990. She received the B.S. degree in geography information science from the Shandong University of Science and Technology, Qingdao, China, in 2012, and the M.S. degree in geoinformation science from The Chinese University of Hong Kong, Hong Kong, in 2013.

She is currently with the Institute of Geographic Sciences and Natural Resources Research, Chinese Academy of Sciences, Beijing, China. Her research interests include the atmospheric remote sensing application and spatial–temporal analysis.